Earth and Planetary Science Letters 605 (2023) 118022

Contents lists available at ScienceDirect

Earth and Planetary Science Letters

journal homepage: www.elsevier.com/locate/epsl

Compactive deformation of incoming calcareous pelagic sediments, northern Hikurangi subduction margin, New Zealand: Implications for subduction processes

Maomao Wang [a,*], Philip M. Barnes [b], Julia K. Morgan [c], Rebecca E. Bell [d], Gregory F. Moore [e], Ming Wang [a], Ake Fagereng [f], Heather Savage [g], Davide Gamboa [h,i], Robert N. Harris [j], Stuart Henrys [k], Joshu Mountjoy [b], Anne M. Tréhu [j], Demian Saffer [l], Laura Wallace [k,l], Katerina Petronotis [m]

[a] College of Oceanography, Hohai University, Nanjing, Jiangsu 210098, China
[b] National Institute of Water and Atmospheric Research, New Zealand
[c] Department of Earth Science, Rice University, Houston, TX, USA
[d] Department of Earth Science & Engineering, Imperial College London, UK
[e] Department of Earth Sciences, University of Hawaii, USA
[f] School of Earth and Environmental Sciences, Cardiff University, UK
[g] Department of Earth and Planetary Sciences, University of California, Santa Cruz, USA
[h] Instituto Português do Mar e da Atmosfera, I.P. (IPMA), Lisboa, Portugal
[i] University of Lisbon, Faculty of Sciences, Instituto Dom Luiz (IDL), Lisboa, Portugal
[j] College of Earth, Ocean and Atmospheric Sciences, Oregon State University, USA
[k] GNS Science, Lower Hutt, New Zealand
[l] University of Texas Institute for Geophysics, Austin, TX, USA
[m] International Ocean Discovery Program, Texas A&M University, College Station, TX, USA

ARTICLE INFO

Article history:
Received 22 August 2022
Received in revised form 12 January 2023
Accepted 22 January 2023
Available online xxxx
Editor: R. Bendick

Dataset link: https://doi.org/10.5281/zenodo.6758019

Keywords:
Hikurangi subduction zone
input sequence
carbonates
compactive deformation
polygonal fault systems
IODP

ABSTRACT

Calcareous rocks are commonly found in subduction zones, but few studies have investigated the consolidation and compactive deformation of these rocks prior to subduction, and their potential effects on subduction and accretionary processes are thus poorly understood. Using drilling data obtained during International Ocean Discovery Program (IODP) Expeditions 372 and 375 combined with 2D and 3D seismic reflection data, the structure, growth history, and slip rates of normal faults identified in the incoming pelagic sedimentary sequences of the Hikurangi Margin were investigated. A seismic coherence depth slice and vertical profiles show that these faults exhibit polygonal structure that has rarely been documented at subduction margins. The polygonal faults are closely spaced and layer-bound within sequences dominated by pelagic carbonate and calcareous mudstone of Paleocene-Pliocene age. Kinematic modeling and 2D displacement analysis reveal that fault throws decrease toward the upper and lower tipline. In detail, two groups of throw profiles are defined by locations of displacement maxima, possibly reflecting lateral variations in physical properties. The polygonal fault system (PFS) likely formed by syneresis processes that involve diagenetically induced shear failure and volumetric contraction of the pelagic unit associated with fluid escape. Fault growth sequences reveal multiple, weakly correlated intervals of contemporaneous seafloor deformation and sedimentation and allow estimates of fault slip rates. We find evidence for a significant increase in typical slip rates from 0.5-3 m/Ma during pelagic sedimentation to >20 m/Ma following the onset of terrigenous sedimentation. These observations suggest that rapid loading of the pelagic sediments by the trench-wedge facies was associated with renewed and faster growth of the PFS. The PFS will eventually be transported into the base of the accretionary wedge, enhancing geometric roughness and heterogeneity of materials along the megathrust, and providing inherited zones of weakness. Selective fault reactivation may facilitate deformation and episodic vertical fluid migration in the lower wedge associated with microearthquakes, tremor, and slow slip events.

* Corresponding author.
E-mail address: wangmm@hhu.edu.cn (M. Wang).

https://doi.org/10.1016/j.epsl.2023.118022

1. Introduction

The structure and seismic behavior of subduction megathrusts may be influenced by the incoming oceanic plate through the effects of seafloor roughness, the composition and physical properties of subduction inputs, and the hydrogeologic and thermal state of the ocean crust (e.g., Underwood, 2007; Spinelli and Wang, 2008; Wang and Bilek, 2011; Saffer and Tobin, 2011; Saffer and Wallace, 2015; Shillington et al., 2015; Kirkpatrick et al., 2020; Hüpers et al., 2017; Barnes et al., 2020). The lithostratigraphy of the subduction inputs is an important variable influencing subduction processes because their material properties and thickness can affect fluid production and permeability and therefore fluid pressure, deformation mechanisms, material strength, and fault slip behavior (e.g., Underwood, 2007; Scholl et al., 2015). Field observations and laboratory experiments reveal that calcareous rocks in particular, including chalks and marls, have different mechanical, frictional, and rheological properties compared to mud-rich siliciclastic rocks (e.g., Ikari et al., 2013; Tesei et al., 2014; Rabinowitz et al., 2018; Boulton et al., 2019; Shreedharan et al., 2022). Faulted calcareous rocks commonly display a range of deformation style and slip localization that reflects the composition of the protolith, including the abundance of clay minerals that enhance pressure-solution of calcite (Gratier et al., 2013a,b), the P-T conditions of deformation, and the relative importance of cataclastic versus diffusive frictional sliding mechanisms (e.g., Tesei et al., 2014; Viti et al., 2014; Boulton et al., 2022). Despite the occurrence of incoming calcareous rocks at many subduction zones (e.g., Plank, 2014), including Hikurangi (Wallace et al., 2019; Barnes et al., 2020), few studies have investigated the incoming pre-subduction consolidation and compactive deformation state of these rocks, and their potential implications for subduction processes remain poorly understood (e.g., Saffer, 2003; Leah et al., 2020; Dutilleul et al., 2020).

In this paper, we build on micro-scale observations made by Leah et al. (2020) by investigating the compactive deformation of incoming (i.e., pre-subduction) pelagic carbonates and calcareous mudstones destined to form part of the plate-interface and accretionary protolith units at the northern Hikurangi subduction zone. We use regional seismic reflection data tied to International Ocean Discovery Program (IODP) Expeditions 372 and 375 borehole petrophysical data and cores from Site U1520 (Wallace et al., 2019; Barnes et al., 2019, 2020) (Fig. 1). We document evidence for widespread, seismic-scale layer-bound polygonal faulting similar to polygonal fault systems (PFS) developed in sedimentary basins at many passive continental margins worldwide (e.g., Cartwright, 2011; Watterson et al., 2000; Gay et al., 2021). Such fault systems typically form in fine-grained sediments with lithologies varying from smectite-rich clays to calcareous mudstones and chalk. These compactive, non-tectonic normal fault systems are characterized by layer-bound host stratigraphy, polygonal structure, small fault displacements, and close fault spacing. Their widespread occurrence in sedimentary basins worldwide has implications for resource exploitation, such as shale gas and gas hydrates, where knowledge of fracture permeability in fine-grained sediments is required (Cartwright, 2011). PFSs have rarely been reported in the input sequences at subduction margins however (Heffernan et al., 2004; Tilley et al., 2021) and their implications for subduction processes are not well studied. We unravel the evolution of these faults in the incoming sequence at north Hikurangi based on analysis of fault growth and discuss the likely mechanism of their formation. We suggest that the faults will impact subduction processes and accretionary wedge development down-dip by contributing geometrical roughness and heterogeneity of materials along the megathrust, providing inherited structural fabrics available for reactivation, and creating potential permeability pathways for fluid flow and pore-pressure modulation.

2. Tectonic and stratigraphic framework

The Hikurangi subduction zone is located on the eastern margin of North Island, New Zealand, where the Pacific Plate subducts beneath the eastern North Island at a rate of 55 mm/yr in our study area (Fig. 1) (Wallace, 2020). The fault structure and slip behavior of the northern sector has been well studied using geophysical methods including geodesy, tomographic imaging, seismic reflection surveys, and passive seismology (e.g., Barker et al., 2018; Bell et al., 2014). The subduction interface hosts some of the shallowest, well-characterized slow slip events (SSEs) (<2-15 km) worldwide, events involving >15 cm of slip occurring at 2-4 year intervals (Wallace, 2020). Historical tsunami earthquakes and tectonic tremor have occurred in the same region, possibly in association with subducting seamounts (Bell et al., 2014; Todd et al., 2018).

The subducting plate comprises the Hikurangi Plateau—a large igneous province of Cretaceous age, characterized by highly irregular seafloor topography and numerous seamounts (Davy et al., 2008; Hoernle et al., 2010; Barnes et al., 2020). At the Hikurangi Trough the Plateau is overlain by a trench wedge of upper Cenozoic siliciclastic sediments overlying older pelagic and volcaniclastic sedimentary rocks of the subducting plateau (e.g., Barnes et al., 2010). The total sedimentary cover sequence thins along the 700 km-length of the margin from ~ 9 km thickness in the south (including up to 6 km of clastic trench wedge) (e.g., Plaza-Faverola et al., 2012; Crutchley et al., 2020) to ~1-1.5 km thickness beneath the northern Hikurangi Trough (Lewis et al., 1998; Barnes et al., 2019, 2020; Gase et al., 2021). In contrast to central and southern sectors, the northern sector is characterized by thinner incoming plate sediments, higher convergence rates (55 mm/yr), and a rougher subducting plate. This change is also associated with a narrower continental margin (60-70 km), relatively limited accretion, and wide areas of frontal tectonic erosion associated with bathymetric re-entrants that resulted from seamount subduction (e.g., Collot et al., 1996, 2001; Lewis et al., 1998; Ellis et al., 2015; Barker et al., 2018; Gray et al., 2019; Barnes et al., 2020; Gase et al., 2021).

In 2017 and 2018, IODP Expeditions 372 and 375 drilled boreholes at Site U1520 in the incoming Hikurangi Plateau (Fig. 1) (Wallace et al., 2019). Site U1520 is located 16 km east of the deformation front and 5 km west of Tūranganui Knoll seamount (Fig. 1). This drilling site, reaching ~1050 m below seafloor (mbsf) in 3520 m water depth, was the first borehole to penetrate the incoming sedimentary sequence in the Hikurangi Trough (Barnes et al., 2020). The stratigraphic section at Site U1520 contains an upper Cenozoic siliciclastic trench-wedge sequence (510 m thick) overlying Paleogene-Neogene calcareous pelagic sediments (340 m thick), which in turn overlie >200 m of upper Cretaceous volcaniclastics (Fig. 2). The succession has been divided into six lithological units (Barnes et al., 2019). The upper most unit, Unit I, contains ~110 m of trench-wedge sandstone-mudstone turbiditic facies. Unit II consists of ~110 m of trench-wedge silty mudstone turbiditic facies interpreted as a mass transport deposit (Lewis et al., 1998). Approximately 290 m of trench-wedge sandstone-silty mudstone turbiditic facies comprises Unit III. Unit IV (~340 m thick) consists of pelagic sediments, including ~ 290 m of marl overlying ~ 50 m of chalk facies. A 168 m thick volcaniclastic conglomerate comprises Unit V, while Unit VI (~30 m) is composed of rocks with mixed characteristics, dominated by interbedded volcaniclastic breccia and mudstone, the base of which was not penetrated. Combining drill core with seismic reflection data reveals that the incoming protolith of the shallow subduction interface straddles the lower part of the pelagic carbonates, the underlying volcaniclastic conglomerates, and an assortment of other volcaniclastic sediments (Barnes et al., 2020; Dutilleul et al., 2020). Our study

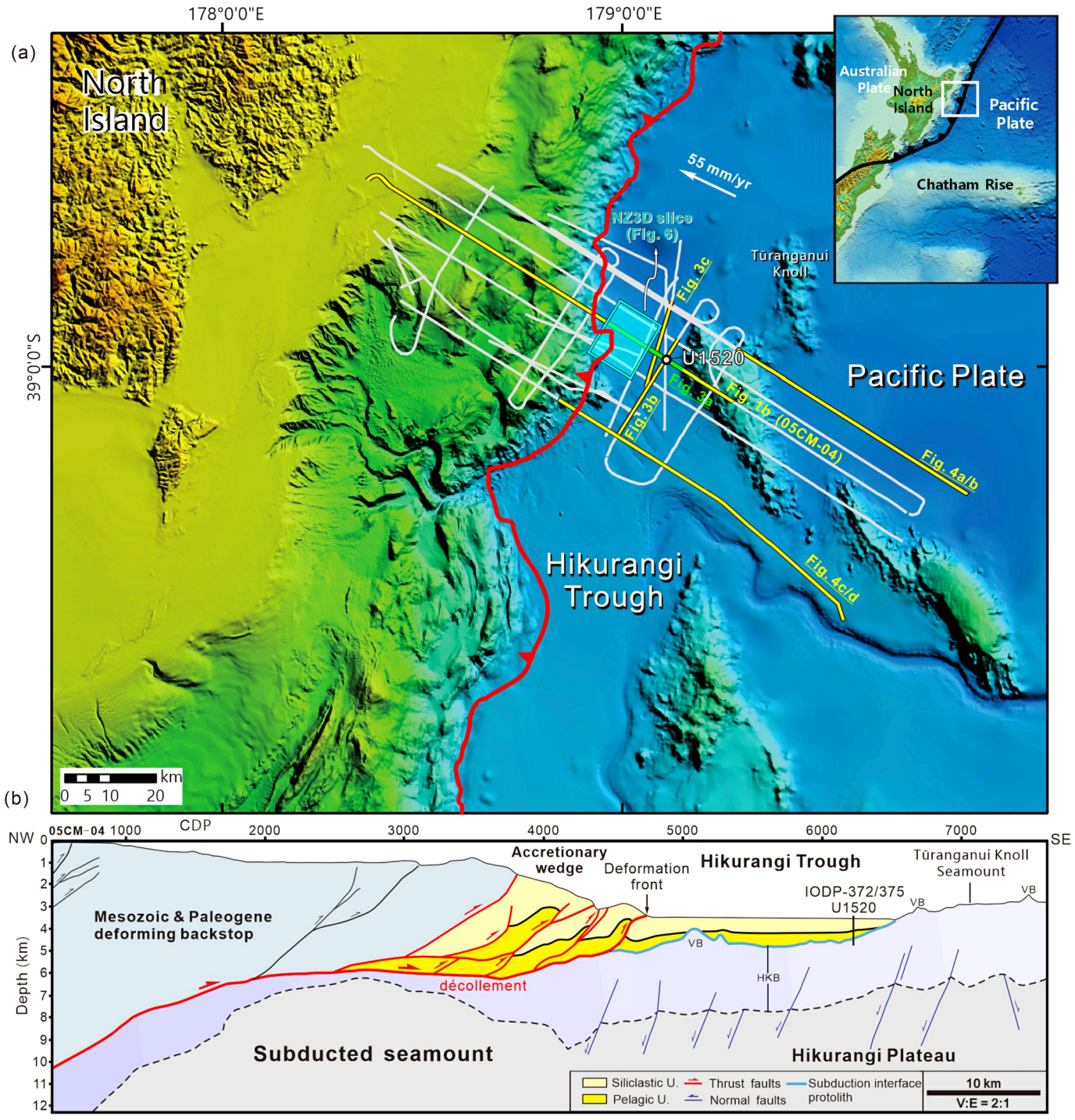

Fig. 1. A) Shaded relief seafloor map showing the bathymetric expression of various structural domains at the northern Hikurangi Subduction Margin, New Zealand. Grey, white, and yellow lines denote the locations of 2D seismic reflection profiles illustrated in this study. Blue shaded rectangle denotes 3D seismic data used in this study. Inset shows tectonic setting of the Hikurangi Trough, and the Pacific - Australian plate boundary. **B)** Interpreted geologic section 05CM-04 showing the structure of the Hikurangi subduction zone west of IODP Site U1520. Structural interpretation is modified from Wallace et al. (2019) and Barnes et al. (2020). Based on the interpretation results from Barnes et al. (2020) and Leah et al. (2020), the stratigraphy of the input sequence is divided into siliciclastic and pelagic lithologies as illustrated by two different color schemes.

focusses on the calcareous pelagic section that is largely accreting and represented by lithological Unit IV (Fig. 2).

3. Data and methods

In this study we present interpretations of five 2D seismic reflection profiles and one 3D seismic coherence depth slice in the incoming plate from the northern Hikurangi Trough and Hikurangi Plateau (see 2D lines and 3D seismic survey locations on Fig. 1a). We also draw on in-situ borehole and core logging information, including structural parameters, porosity, and P-wave velocity (Fig. 2) (Wallace et al., 2019; Barnes et al., 2019; Dutilleul et al., 2020).

The 2D seismic data include profiles 05CM-04 (Fig. 3a), TAN1114-04 (Fig. 3b), RR1508-HKS01-01 (Fig. 3c), MGL1708-MH24 (Fig. 4A/B), and TAN1114-11 (Fig. 4C/D) (uninterpreted version on Supplementary Figs. S1-S5). The seismic coherence depth slice and

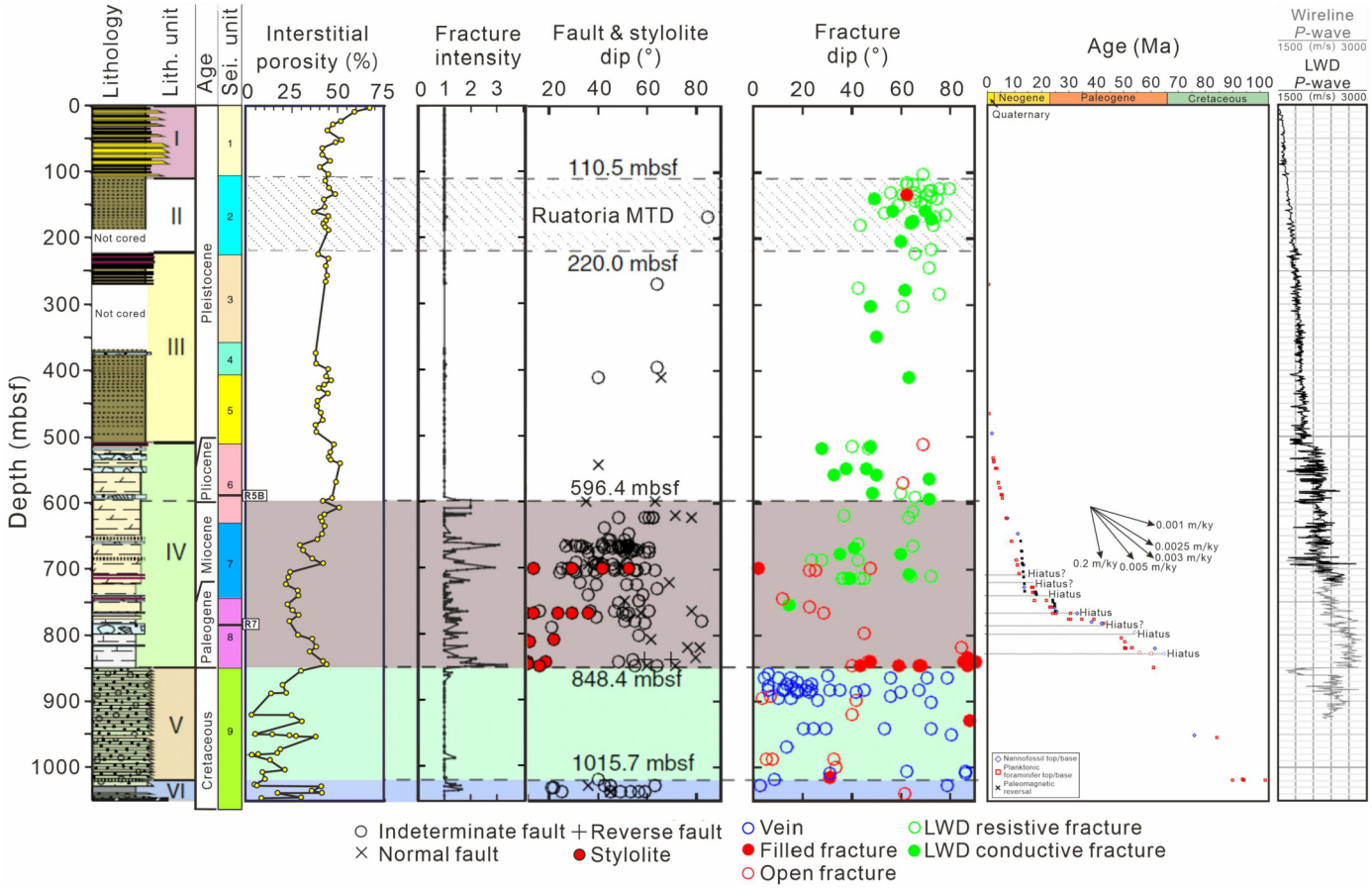

Fig. 2. Lithostratigraphy, seismic units, interstitial porosity, fracture intensity, structure, and *P*-wave velocity (wireline and LWD) for IODP Site U1520 (Wallace et al., 2019; Barnes et al., 2019; Dutilleul et al., 2020). LWD: logging while drilling. On the seismic unit column, the two horizontal bold black lines with labels R5B and R7 are additional horizons used in this study. Age control is derived from biostratigraphic and paleomagnetic data of Barnes et al. (2019) and Crundwell and Woodhouse (2022). In fracture dip columns, white shading is defined by sub-horizontal to gentle dipping beds, gray shading is defined by calcareous, clay-rich sediments in Unit IV with extensive faults and dissolution, green shading is defined by common zeolite and carbonate veins and coincides with volcaniclastic Lithostratigraphic Unit V, light blue shading is characterized by heterogeneous lithologies, including highly altered volcaniclastics in which deformation is dominated by minor faults.

an additional supporting 2D profile are derived from a 3-D seismic volume collected in 2018 ("NZ3D survey"; Fig. 5) (Han et al., 2021; Moore et al., 2021). Profile 05CM-04, crossing IODP Site U1520, was acquired by the New Zealand Government in 2005 with a 4140 m^3 air-gun source array and a 12 km hydrophone streamer consisting of 960 channels (Barker et al., 2018). A seismic-well tie at Site U1520 was developed by Barnes et al. (2019) to correlate physical property changes in geophysical logging, lithology, and core physical properties with the seismic reflection data. The depth-converted profile has a vertical resolution of ~15 m from ~500 to 700 mbsf, ~18 m from 700 to 900 mbsf, and ~25 m from 900 to 1200 mbsf (Barnes et al., 2019).

Profiles TAN1114-04, TAN1114-04-11 and RR1508-HKS01-01 were acquired on the RV *Tangaroa* survey TAN1114 in 2011 and R.V. *Roger Revelle* survey RR1508 in 2015, respectively (see Supplementary file for reference to data acquisition and processing information). The TAN1114 data has a vertical resolution of ~8 m for seismic units SU4 and SU5, 10 m for units SU6, SU7 and the upper part of SU8 (above horizon R7), and 11 m for the interval of unit SU8 beneath R7 (Figs. 3 and 4). The RR1508 data has a vertical resolution of ~5 m for seismic units SU4 and SU5, 6 m for units SU6, SU7 and the upper part of SU8 (above horizon R7), and 7 m for unit SU8 beneath R7. For display of these sections in Fig. 3b and c, we converted the data to depth using a nominal interval velocity of 2000 m/s. Line MGL1708-MH24 was acquired with a multi-channel seismic system on RV *Marcus Langseth* during the 2D SHIRE survey MGL1708 (e.g., Gase et al., 2021). Data acquisition consisted of a tuned 36 air-gun source array with a total volume of 6,600 in3 and a 1008 channel streamer with a group spacing of 12.5 m. The source spacing was 37.5 m and the record length 14 s. The data were processed using a bin size of 6.25 m, with application of de-noise and deconvolution prior to normal moveout correction and post-stack Kirchhoff migration. Post-migration data conditioning included a Ormsby bandpass filter, and automatic gain control. The polarity of all seismic sections, and any seafloor mis-ties between them, were adjusted to match the 05CM-04 data.

We utilized a 14×12 km^2 seismic coherence slice obtained from the NZ3D experiment (Figs. 5, S6, see locations on Fig. 1a) (Han et al., 2021; Moore et al., 2021). This seismic slice was extracted from a 3D pre-stack time migrated seismic data volume with a total survey area of 14×60 km^2 acquired in 2018 by the RV *Marcus Langseth*. Seismic coherence, based on comparison of waveforms across adjacent traces, gives apparent continuity to discontinuous features, such as faults and edges, irrespective of their orientation (Bahorich and Farmer, 1995). The values of seismic coherence are between 0 (no similarity between adjacent traces) and 1 (adjacent traces are identical). Because faults generate surfaces of low coherence, this attribute is particularly useful for identifying polygonal faults (e.g., Cartwright, 2011). The seismic data were recorded in 9.5-s long records with a sampling rate of 2 ms. Additional information about acquisition of the 3D seismic data are presented by Han et al. (2021).

We correlated the basal horizon of nine seismic stratigraphic units (SU1-SU9) identified by Barnes et al. (2019) on profile 05CM-

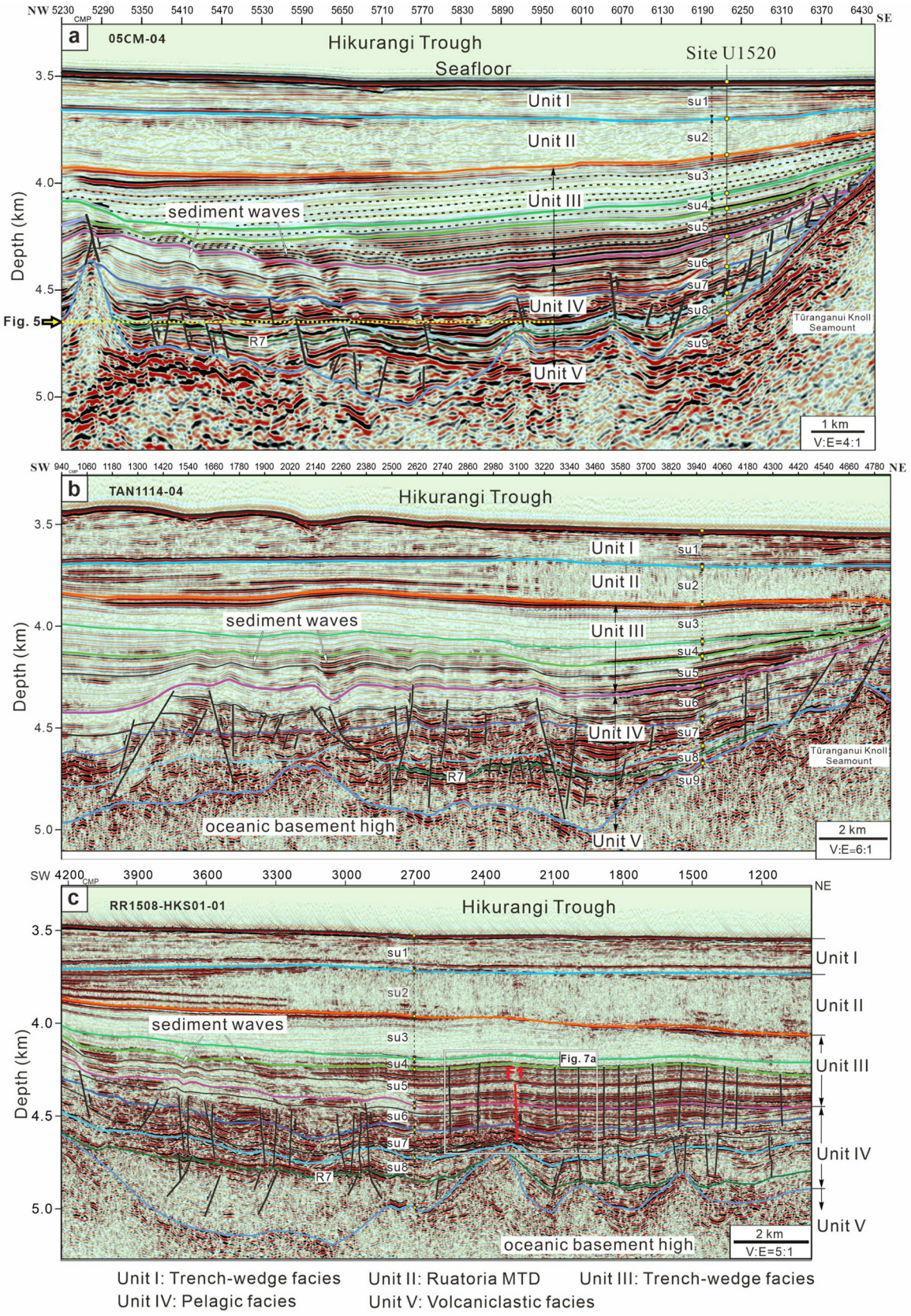

Fig. 3. Interpreted depth converted seismic reflection profile 05CM-04 (Fig. 3a), TAN1114-04 (Fig. 3b), and HKS01-01 (Fig. 3c) imaging the incoming sedimentary sequences and layer-bound normal faults in the pelagic section beneath the Hikurangi Trough. See locations on Fig. 1. Migrating sediment waves within seismic unit SU5 are annotated. The yellow dashed line in Fig. 3a indicates the location of the seismic coherence slice in Fig. 5. The fault F1 in red color in Fig. 3c was selected for kinematic modeling with *StructureSolver* (see Fig. 6).

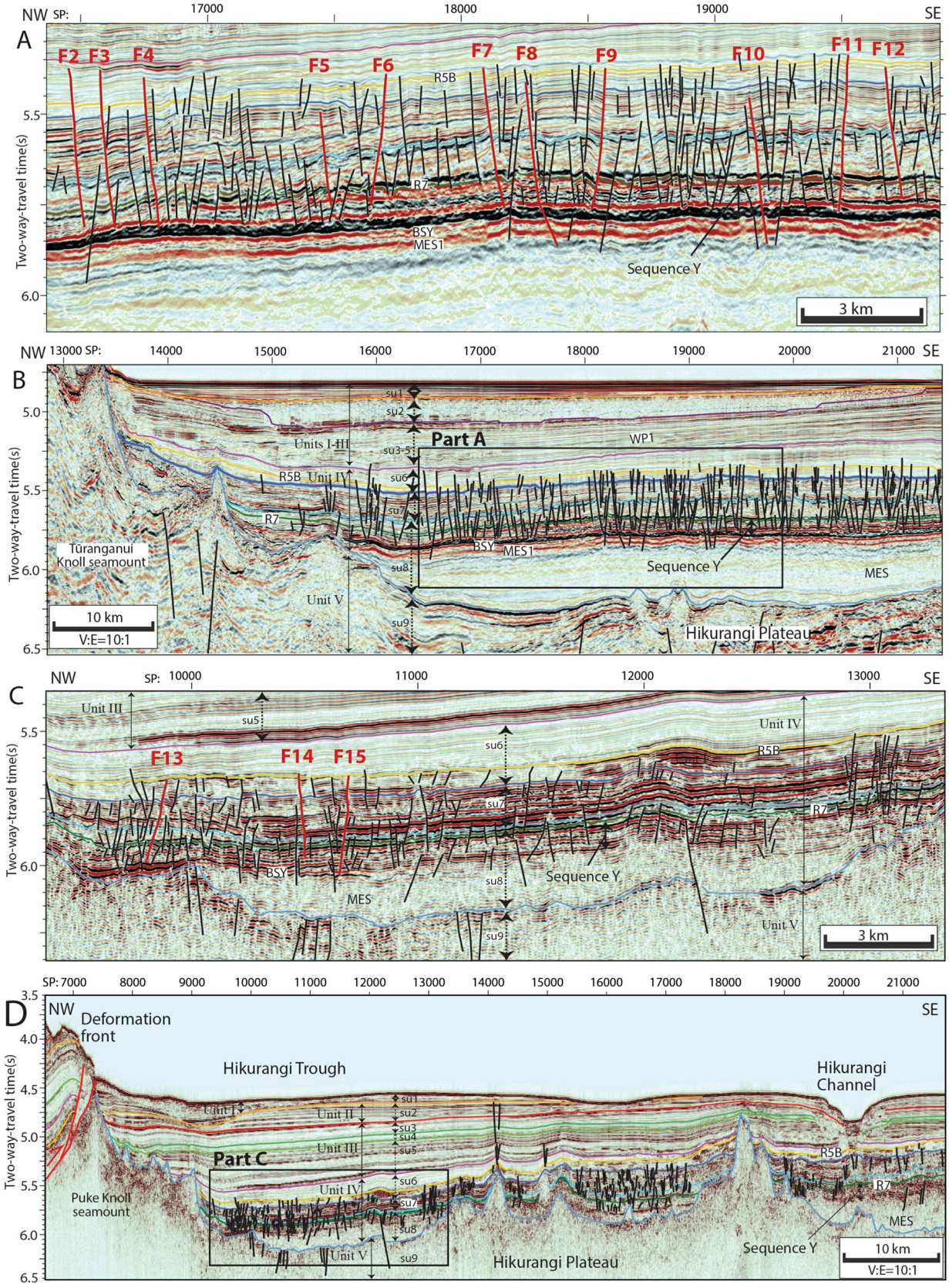

Fig. 4. Interpreted time migrated seismic reflection profile MGL1708-MH24 (A, B) and Tan1114-11 (C, D) imaging the incoming sedimentary sequences and layer-bound normal faults in the pelagic section beneath the Hikurangi Trough. See line locations on Fig. 1. Faults in red color with labels F2 to F15 are those selected for displacement analysis (see Fig. 7 and Figs S7-S10).

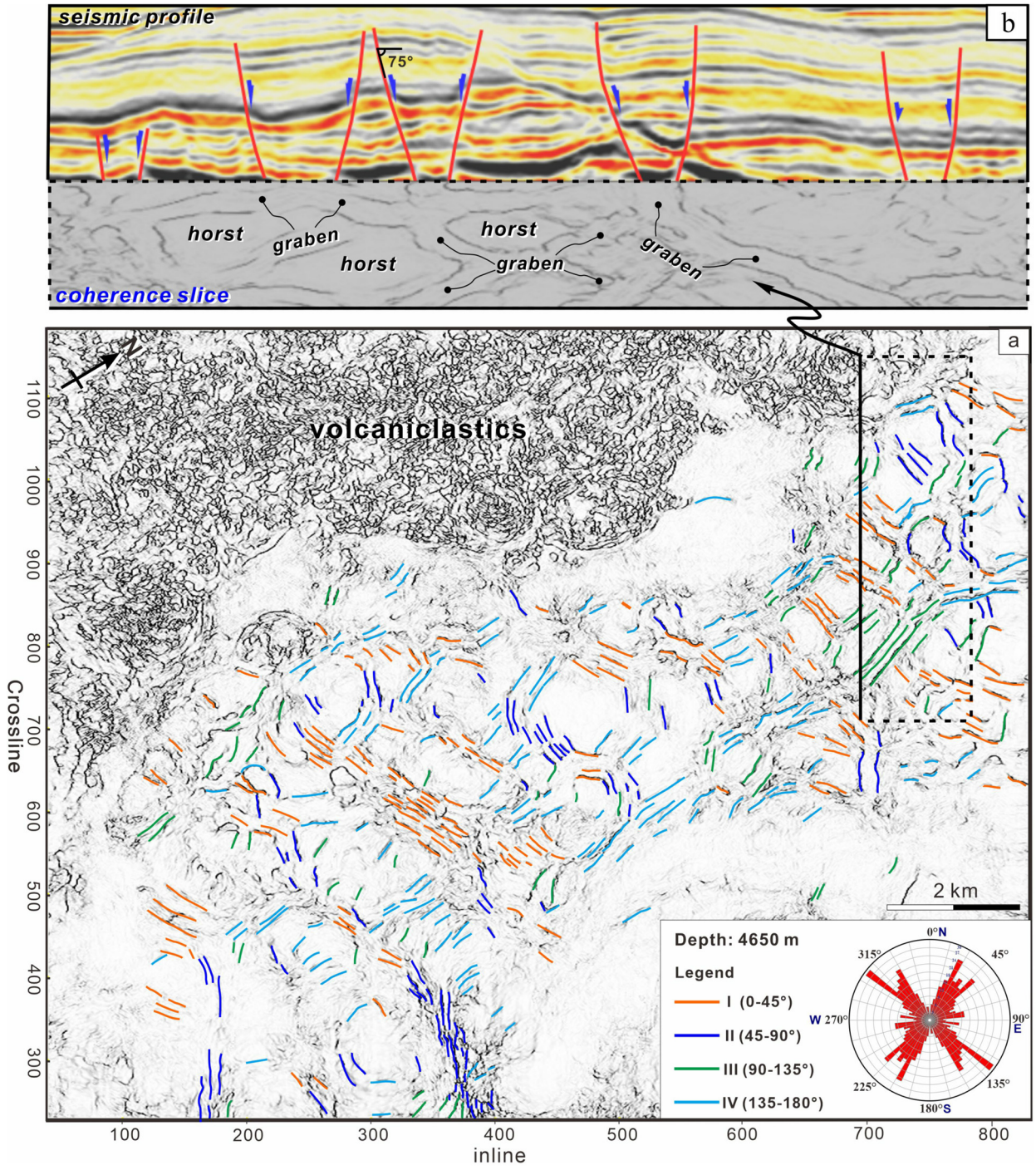

Fig. 5. (a) Seismic coherence slice at 4650 m showing clear expression of polygonal fault systems in the incoming pelagic calcareous sequence. This seismic coherence slice is extracted from the 3D seismic cube of NZ3D volume (Han et al., 2021; Moore et al., 2021). For location of this slice, see 3D seismic area in Fig. 1a. Note rotation of the North arrow. The yellow, blue, green and cyan lines represent the azimuth of the fault segments in the PFS. Inset is rose diagram of the fault segment orientation in the PFS. (b) Integration of horizontal seismic coherence slice and vertical seismic profile. The locations of graben and horst are labeled on the coherence slice.

04 at Site U1520 (Fig. 2) onto the TAN1114 and RR1508 lines, and where possible onto the MGL1708 section (Figs. 3 and 4). Seismic units SU5 to SU8 are of particular significance, encompassing the lower part of the trench wedge siliciclastic succession and the underlying pelagic calcareous sediments (Fig. 2). On Fig. 4 we also identify Sequence Y, a seismic unit bound by horizons R7 and BSY and correlated widely across the Hikurangi Plateau (Davy et al., 2008) and along the Hikurangi Trough (Barnes et al., 2010). Sequence Y is a prominent, continuous high-amplitude reflection package that consist of early Oligocene to Late Cretaceous mudstone and chalk (Davy et al., 2008). At IODP Site U1520, Sequence Y represents the lower part of SU8, is 72 m thick, and comprises Middle Eocene to Early Paleocene chalk. For fault displacement analysis in this study we estimated the ages of seismic marker horizons (Figs. 3 and 4) using biostratigraphic and paleomagnetic datums at IODP Site U1520 (Barnes et al., 2019; Crundwell and Woodhouse, 2022) (Fig. 2), supported by regional seismic interpretations of Davy et al. (2008) as follows: WP1 (Fig. 4B), 0.5 ± 0.2 Ma; base SU5, 1.85 ± 0.2 Ma; R5B, 5.08 ± 0.3 Ma; base SU6, 9.09

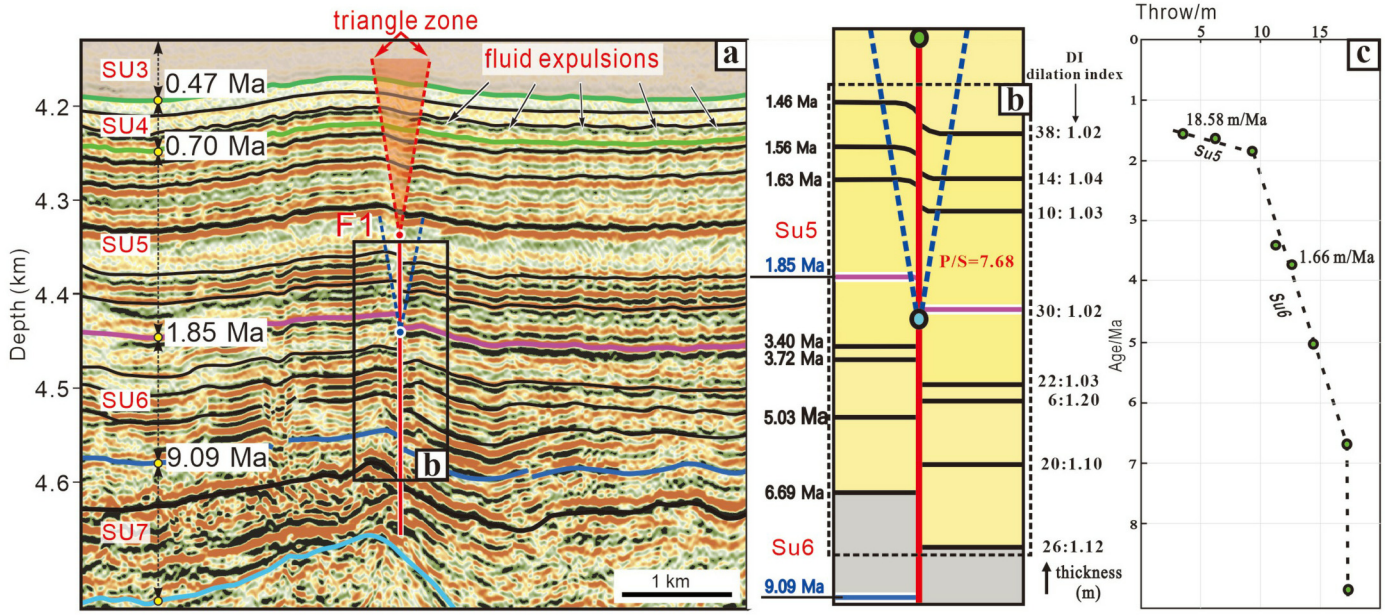

Fig. 6. (a) Details of high-resolution depth converted seismic reflection profile RR1508-HKS01-01 (Fig. 3c) highlighting fault F1 and other seismic features associated with fluid expulsion in upper Unit IV and lower Unit III. SU3-SU7, seismic units. (b) Best-fitted model for fault F1, computed with Trishear software, *StructureSolver* (Eichelberger et al., 2017), assuming trishear normal fault-tip propagation kinematics. DI = Dilation index. If the DI value is equal to 1, it indicates that the fault was inactive during this interval and the hanging wall did not receive enhanced deposition relative to the footwall; if the DI is greater than 1, it indicates that the fault was active, and the hanging wall underwent enhanced syn-kinematic deposition. P/S = propagation to slip ratio. (c) Plot of age versus throw of different layers in Fig. 6a & b.

± 0.1 Ma; base SU7, 23.08 ± 0.2; R7, 40.1 ± 1.0 Ma, BSY, 70 ± 3.0 Ma; and MES1, 75 ± 3.0 Ma.

The locations and displacements of normal faults in the incoming pelagic section were identified primarily from fault cutoffs and stratigraphic correlations. We selected 15 representative faults (F1 to F15) for detailed 2D displacement analysis and structural modeling (Figs. 3 and 4). We analyzed the displacement profiles with depth along with the syntectonic fault growth strata using measurements from the adjacent footwall and hanging wall sequences to determine the displacement characteristics, timing of activity, and fault slip rates (e.g., King and Cartwright, 2020) (see Supplementary Figs. S7-S10). The geometry of growth strata is controlled by contemporaneous seafloor deformation, fault-propagation folding, and the ratio of sedimentation/throw rate.

To model the development of fault F1 (Figs. 3c, 6) we used *StructureSolver version 4.2*, a kinematic forward modeling and restoration software package (Eichelberger et al., 2017). The dilation index (DI) in *StructureSolver* indicates the ratio of the hanging wall to the footwall thickness, which can be used to reflect the fault activity and the timing of syn-kinematic deposition. For each of faults F2 to F15, we measured the vertical separation (throw) of positive phase reflections in the footwall (FW) and hanging wall (HW) panels on time sections, and where present, identified the structural relief associated with fault-propagation flexures indicative of monoclinal folding above blind fault tips. Small fault separations can be measured confidently to at least half a seismic wavelet. Although the seismic profiles displayed in Figs. 3b and 3c were depth converted using a nominal interval velocity (Vp int) of 2000 m/s, a more detailed 1D velocity structure was used to convert the horizon positions and fault vertical separations to depth for fault displacement analysis. Based on the Vp logs from drilling data (Fig. 2), interval velocities range from 1.7-2.1 km/s for the lower 100 m of the clastic section above horizon BSU5, 1.7-2.8 km/s between BSU5 and R7, and 2.3-2.9 km/s below R7 (Supplementary Fig. S7). We also consider the lateral variation in Vp on profile 05CM-04 obtained by the full waveform inversion away from Site U1520 (e.g., Gray et al., 2019). In order to capture the bulk of the unit velocities for depth conversion, we filtered outliers at extreme values and set the error estimates and the average interval velocities of the three corresponding layers mentioned above to 1.9 ± 0.2 km/s, 2.3 ± 0.3 km/s, and 2.7 ± 0.5 km/s, respectively. This results in uncertainty in the vertical separation measurements of ~10-20% (Figs. 7, S7, S9). We then calculated the vertical separations with depth normalized to the maximum throw (Supplementary Fig. S8), plotted measurements of throw versus geologic age to determine fault growth history (Supplementary Fig. S9), and calculated slip rates (Supplementary Fig. S10). The above errors in interval velocities have little impact on the calculated vertical separation rates (Figs. 7, S10).

4. Basin-scale seismic stratigraphy

The structural and stratigraphic architecture of the northern Hikurangi margin and subducting plate are illustrated in Fig. 1b, while details of the incoming Hikurangi Trough seismic stratigraphy are presented in Figs. 3–6. The majority of the Hikurangi Trough sedimentary sequence onlaps the flank of Tūranganui Knoll seamount (Fig. 3). The sequence contains five stratigraphic units, Units I, II, III, IV, and V, corresponding to seismic units SU1, SU2, SU3-5, SU6-8, and SU9, respectively (Fig. 2). The seismic units SU1 to SU5 comprising predominantly siliciclastic turbidites and hemipelagic sediments of Pleistocene to Recent age (lithologic Units I to III) (Barnes et al., 2019) are mostly characterized by continuous seismic reflections (Figs. 3–4). Seismic unit SU2 (Unit II) exhibits an acoustically chaotic internal structure that corresponds to the seismic stratigraphic characteristic of mass transport deposits (MTDs) and represents the distal region of the Ruatoria mass-flow in the north Hikurangi margin (Figs. 3, 4 A-B). Notable is the occurrence of migrating sediment waves within seismic unit SU5 (Sections a, b, c in Fig. 3).

Seismic units SU6 to SU8 (i.e., Unit IV) comprising pelagic calcareous sediments are sub-horizontal beneath the center of the basin and rise gently towards areas of positive relief on the underlying volcaniclastics unit, including Tūranganui Knoll seamount and a smaller buried seamount beneath the center of the trough (Figs. 3–4). Reflections within these units are generally more irreg-

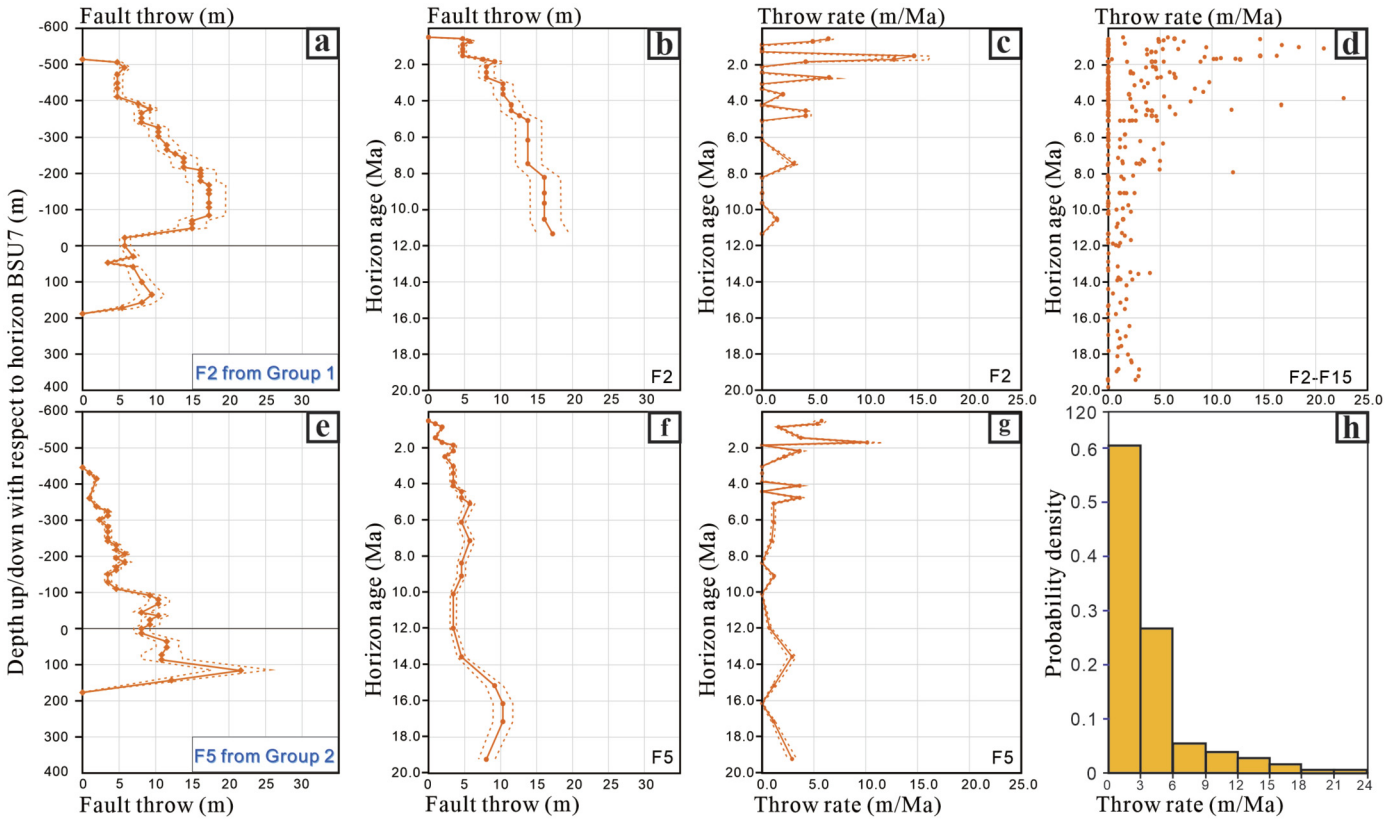

Fig. 7. (a), (e) Plot of fault throw versus depth up/down with respect to horizon BSU7 for faults F2 and F5, respectively. (b), (f) Plot of fault throw versus horizon age for faults F2 and F5, respectively. (c), (g) Plot of throw rate versus horizon age for faults F2 and F5, respectively. (d) Plot of fault throw rate versus horizon age for 14 polygonal faults from F2 to F15 (see locations on Fig. 4). (h) Probability density function of throw rates for 14 polygonal faults. The dashed line indicates the error estimation of the calculation results.

ular and discontinuous than in the overlying clastic section, and reflection amplitudes vary greatly (Figs. 3–4).

At Site U1520 and further east, reflections in seismic unit SU6 (511–631 mbsf) are moderate to low amplitude and are disrupted (section a in Fig. 3). Core lithologies indicate light greenish gray calcareous mudstone of late Miocene to early Pleistocene age with minor beds of volcanic tuff, and chaotic debris flow deposits (common in the upper 90 m) that originated from the flank of Tūranganui Knoll (Barnes et al., 2019). Relative to the lower part of the overlying clastic section these sediments reveal a significant drop in gamma ray values (~20-50 gAPI, indicative of reduced clay content (~20-45%), associated with an increase in calcite content (~40-70%) and higher *P*-wave velocities (~2100-2300 m/s) (Fig. 2). Immediately west of Site U1520, the reflections transition to higher amplitudes, are more continuous, and grade into the lower part of the sediment waves beneath the center of the trough (section b in Fig. 3). Seismic unit SU7 (631-745 mbsf at Site U1520) is characterized by mixed but generally higher reflection amplitudes, discontinuous reflections, reduced porosities (30-40%), and higher velocities (typically 2100-2500 m/s) (Fig. 2). At Site U1520, the unit has highly variable, discontinuous reflections, and comprises brownish marl and calcareous mudstone with rare intervals of matrix-supported debris flow deposits, volcanic tuff, and volcaniclastic siltstone of early to late Miocene age. Normalized calcite percentage in these sediments is comparable to seismic unit 6, as are logged gamma ray values (Barnes et al., 2019).

The lower part of the pelagic calcareous succession, seismic unit SU8, is characterized by generally strong, discontinuous reflections (Figs. 3–4). At Site U1520 (745-850 mbsf), the unit is relatively weaker acoustically, with reflections onlapping the underlying volcaniclastic unit SU9 (Fig. 3). The cored lithologies comprise marl, calcareous mudstone and chalk of late Paleocene to early Miocene age, with minor carbonate debris flow deposits (Barnes et al., 2019). The chalk, below seismic horizon R7, exhibits low gamma ray values (~20 gAPI) and higher *P*-wave velocities (2600-2800 m/s) in logging-while-drilling data, the lowest porosities of the entire calcareous sequence, and the highest calcite content (up to 90%) in cores (Dutilleul et al. (2020). To the south and east of Tūranganui Knoll seamount seismic unit SU8 includes reflection R7 at the top of a prominent high-amplitude package of reflections that have been recognized regionally as Sequence Y (Davy et al., 2008; Barnes et al., 2010) (Fig. 4). Beneath Sequence Y and above plateau volcaniclastics is a widespread acoustically weak unit MES (absent at Site U1520) that may comprise siliciclastic sediments of Cretaceous age (Davy et al., 2008).

5. Fault structure and slip rates

In all 2D seismic profiles (Figs. 3, 4), we observe a prominent layer-bound array of dense, high-angle normal faults developed within the Cenozoic pelagic carbonate and calcareous mudstone succession. These faults have mixed dip directions with opposing faults converging at depth. Most of the faults are stratigraphically confined to seismic units SU6 - SU8 (lithological Unit IV), although some appear to extend into and/or be associated with folding of the overlying siliciclastic cover (seismic units SU5 and possible SU4, in Unit III) (Figs. 3c, 4, and 6). Where faults extend into the siliciclastic cover (SU5 and SU4) they are locally manifested as sub-vertical weakly reflective zones that offset seismic reflections (Figs. 3c and 6, Supplementary Fig S3). Such weak reflection zones are commonly interpreted to be correlated with fault-related fluid migration, as reported in other sedimentary basins worldwide (Berndt et al., 2003; Cartwright, 2011).

The seismic sections reveal the fault network to be largely independent of and isolated from relief on the underlying volcaniclastics, and this is notably apparent in areas where sequence MES is inferred (Fig. 4A, B). We note that minor, localized extensional faulting occurs in the siliciclastic cover above positive relief on the underlying volcaniclastics (e.g., Fig. 4D), and in rare instances faults may extend downwards into high-relief areas of the underlying volcaniclastics where sequence MES is thin or absent, however the irregular nature of the upper volcaniclastic contact makes interpretation of their down-ward continuity ambiguous (Fig. 4).

In depth-converted 2D seismic sections the majority of the faults are steeply dipping (for instance, an apparent fault dip of 75° is shown in Figs. 5a), planar to gently curved, and have small displacements generally in the range of a few meters to <30 m. The faults have profiles with displacement maxima in the calcareous mudstones diminishing with depth towards the upper and lower tips, and two groups of displacement profiles are recognized (Figs. 7 and supplementary Figs S7-S8). Group 1 fault profiles exhibit displacement maxima in the Miocene seismic units SU6 and SU7, and a secondary maxima in the Oligocene part of unit SU8 (Supplementary Fig. S8A & C). The relatively low displacement between the two maxima is here considered to be real, while its absolute magnitude may be affected slightly by the uniform velocity applied through this interval (2.3 km/s) in depth conversion of the displacement data. Group 2 fault profiles are characterized predominantly by a displacement maxima in the Paleogene sequence SU8 (Supplementary Fig. S8B & D), and appear to be confined spatially to the central area on Fig. 4a where the interval R7-BSY has relatively higher seismic amplitudes than in the adjacent areas to the NW and SE.

A coherence slice and vertical profile acquired from the NZ3D seismic volume reveals the planform geometry of the faults in Unit IV at a depth of 4650 m. As shown in Figs. 5a, the central region of the coherence slice clearly demonstrates the polygonal geometry of the faults in the calcareous sequence, which contrasts strongly with the internal acoustic characteristics of the underlying volcaniclastics on both sides of the image slice (Figs. 5, uninterpreted version on Fig. S6). We selected one area (see dashed box in Fig. 5a) of the coherence slice and combined it with a corresponding vertical seismic profile from the NZ3D volume to illustrate the 3-dimensional structural geometry (Fig. 5b). Our interpretation shows that five pairs of graben structures are developed on the vertical profile, each consisting of two normal faults with opposite dips. These graben structures coincide with the rims of narrow, ring-like structures imaged on the seismic coherence slice, while the horst structures are consistent with the core areas in the PFS (Fig. 5b). We distinguish four groups of differing fault strikes in plan view on the time slice at 4650 m (shown by four colors on Fig. 5a), from 0° to 180°. The rose diagram of fault segment strikes indicates that the PFS comprises two relatively dominant fault strike sets, NE25-30° and SE125-130°, respectively. The polygonal structures in plan view include hexagons, pentagons, and quadrilaterals. At this depth, the polygon structures are about 0.4-0.2 km wide and range in length from 0.5-1.1 km. These geometries are similar to PFSs that are widely reported to occur in fine-grained sedimentary sequences in many passive continental margin basins (e.g., Cartwright, 2011). In contrast, the coherence data from the volcaniclastic unit reveals a chaotic seismic reflection pattern with no dominant strike of faults and fractures (Figs. 5a).

Our kinematic modeling of fault F1 using *StructureSolver* reveals an overall structural style conforming to the geometry of a normal tri-shear fault and a fault-propagation fold with a triangular shear zone interpreted above the fault tip (Fig. 6) (Eichelberger et al., 2017). The fault throw range is 3.5-17.3 m, while the apparent dip angle in Fig. 6 is ~88 degrees, indicating the fault throw is approximately equivalent to the fault slip. The measured DI ranges from 1.0 (no growth) to 1.20 and reveals a non-linear growth history (Fig. 6). Two phases of syn-kinematic deposition and fault growth are recognized on fault F1, mainly in the calcareous mudstones of seismic unit SU6 and the lower part of the overlying siliciclastics (SU5-SU4), respectively. The first growth phase occurred between 6.69 to 1.85 Ma. The second occurred between 1.85 to 0.47 Ma and was dominated by upward propagation of the fault tip and trishear folding of the overlying growth strata. The growth stratigraphy indicates that the contemporary deformation affected the seabed, influencing sedimentation loci. Based on the structural modeling and growth stratigraphy, we calculated a slip rate of about 1.66 m/Ma for the first stage of fault F1's development and 18.58 m/Ma for the second stage (Fig. 6c).

The non-linear growth history of fault F1 indicated by the above kinematic modeling is also supported by our detailed 2D displacement analysis of faults F2 to F15 (Figs. 7; and supplementary Fig. S10). The throw vs age profiles (Figs. 7b, f, and supplementary Fig. S9) commonly reveal an increase in slip rate from 0.5-3.0 m/Ma during pelagic sedimentation (20-1.85 Ma) to over 20 m/Ma following the onset of siliciclastic sedimentation since 1.85 Ma. Furthermore, the plots reveal multiple weakly correlated intervals of fault growth separated by quiescent intervals with no growth (Figs. 7c, g, supplementary Fig. S10), the duration of these intervals appears to be variable and of the order of 10^5-10^6 yrs.

6. Discussion

6.1. Polygonal faults in the incoming calcareous pelagic sediments

The incoming calcareous pelagic sediments approaching the northern Hikurangi subduction margin have distinctive lithological, structural, and physical properties compared to the overlying and underlying formations. The carbonates and calcareous mudstones are characterized by porosity that decreases with depth from ~40%–50% in seismic unit SU6, and ~20%-43% in unit SU7, to ~20%–45% in unit SU8 (Fig. 2) (Dutilleul et al., 2020), and by confined normal faults that are indicative of brittle deformation. Leah et al. (2020) demonstrated that in addition to bulk compaction, porosity loss is concentrated in stylolites at the cm-scale. In this study, based on 2D- and 3D-seismic reflection data, we find that the incoming pelagic succession also exhibits structures characteristic of PFSs (Cartwright, 2011). These faults are characterized by: 1) layer-bound structural confinement; 2) fine-grained sedimentary host; 3) moderate to steep dips; 4) converging and intersecting structure; 5) limited displacement (typically <30 m); 6) very slow rates of growth, and 7) polygonal geometries in plan view. Such features combined with the development of sub-horizontal stylolites and clusters of small normal faults at core scale (Leah et al., 2020) have been attributed to gravitational loading of fine-grained sediments, mechanical consolidation, syneresis involving diagenesis and volumetric contraction (rather than extension), and expulsion and migration of pore fluids, possibly through the PFS (e.g., Cartwright, 2011).

Layer-bound PFSs have been widely reported within sedimentary basins (e.g., Cartwright, 2011; Berndt et al., 2003; Gay et al., 2004; King and Cartwright, 2020). Most published examples of this structural style are from sedimentary basins in passive continental margin settings, where 3D seismic datasets have revealed layer-bound intersecting extensional faults ranging from well-developed polygonal networks to discontinuous patches of polygonal faults connected by intersecting linear structures (e.g., Watterson et al., 2000). Locally, the specific structural styles at horizon level or depth slice in PFSs depend on stratigraphic position, lithology, physical properties, the evolutionary stage of the fault system development, and the magnitude of displacement (e.g., Cartwright,

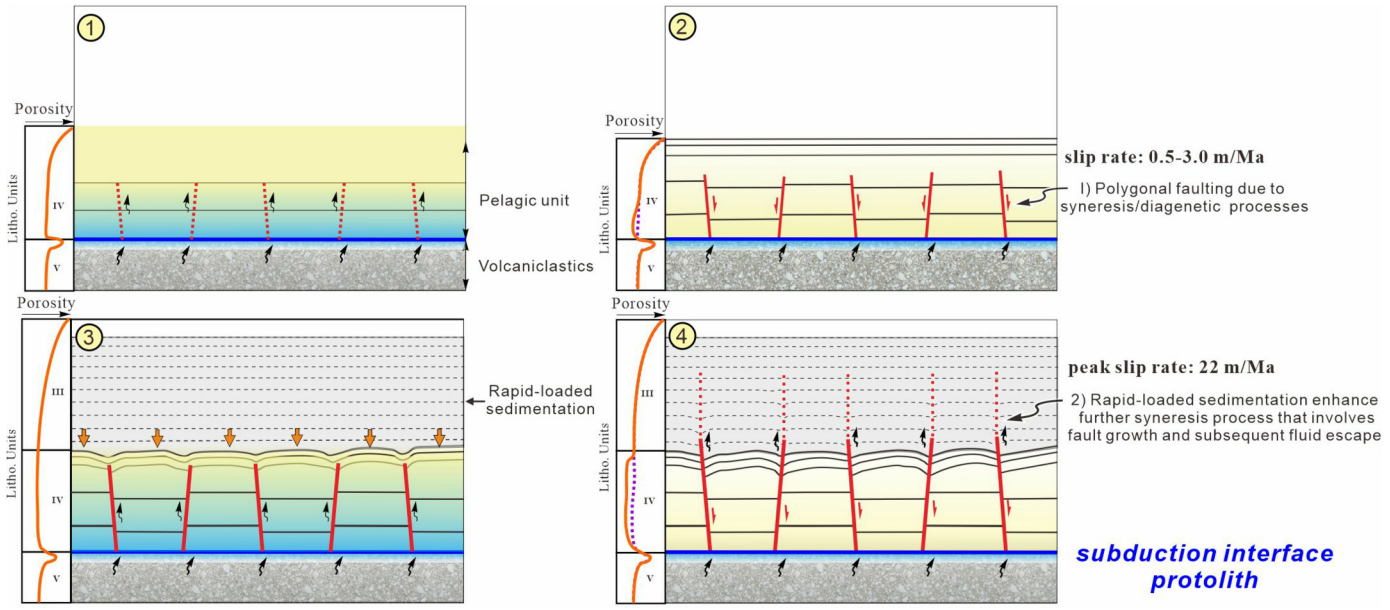

Fig. 8. Schematic model of sequential evolution of the formation of polygonal normal faulting in the pelagic calcareous sediments followed by rapid loading of the trench-wedge section in the Hikurangi Trough. Columns on the left indicate relative porosity changes within Lithological Units III to V.

2011). Planform and vertical profile displacement–depth and distance relationships of these faults globally exhibit similarities to those of tectonic normal faults. However, recent studies have shown that the slip rates of active polygonal faults are 2–3 orders of magnitude smaller than those of tectonic and gravity-driven extensional faults in passive margins (King and Cartwright, 2020).

From our analysis of fault growth, we infer fault nucleation approximately at the stratigraphic levels of the displacement maxima, followed by progressive upwards and downwards propagation of the fault tips coeval with syn-kinematic deposition. Faults F2-F15 reveal multiple intervals of growth stratigraphy separated by intervals with an absence of growth strata, spanning timeframes of 10^5-10^6 yrs. Weak temporal correlation of specific growth intervals across the fault array combined with lateral variations of throw rates (Fig. S10) may indicate temporal and spatial variability in the development of specific faults and polygonal cells. The factors leading to the two identified groups of fault displacement with depth profile (Figs. 7 and S8) remain unclear. However, our observations of accompanying lateral variations in seismic amplitudes within the pelagic stratigraphic intervals, combined with lateral variations in Vp reported elsewhere (Gray et al., 2019), may indicate that both spatial and stratigraphic variations in physical properties influence the precise loci of fault nucleation and displacement maxima. This is supported by the observations of Dutilleul et al. (2020), who demonstrated that the proportion of hydrous versus non-hydrous minerals in different intervals has a strong control on the physical properties, and that concentrated zones of core-scale faulting within calcareous mudstones of seismic units SU7 and SU8 are associated with intervals of relatively higher calcite percentage and *P* wave velocity along with reduced porosity and permeability.

Our analysis supports the interpretation of King and Cartwright (2020) that polygonal faults form at extremely slow slip rates ranging from 0.5 to 20 m/Ma (Figs. 7d, S10). We also suggest that the rapid accumulation of the siliciclastic trench wedge in the Pleistocene was followed by the renewed propagation of the faults into SU5. The absence of both a regional protothrust overprint across the trench seismic sections (Figs. 3 and 4) and of borehole breakouts at IODP Site U1520 (Barnes et al., 2019) imply that the incoming trough sequence remains in a state of uniaxial loading. The ongoing burial of the lower section was likely accompanied by further expulsion of pore fluids at seismic and sub-seismic scales (see SU6 and SU5 in Figs. 4, 6 and S3) through exploitation of polygonal fault and fracture permeability.

In our seismic data, the steeply-dipping, weak reflection zones in the upper reaches of the faults or above their tips (Fig. 6), are consistent with the fault-related fluid migration reported in other sedimentary basins worldwide (Berndt et al., 2003; Cartwright, 2011). These features are also consistent with the observed clay seams and breccia associated with the core-scale faulting at Site U1520 (Leah et al., 2020). Considering the observed upwards increase in fault slip rates (Fig. 7d), we infer that the rapid loading of trench-wedge siliciclastics during the Pleistocene may have enhanced further volumetric contraction in and below the pelagic sediments (Fig. 8), which in turn resulted in further brittle deformation and transient fluid expulsion from these sequences. The steep, weakly reflective features, combined with core- and micro-scale evidence of fluid migration (Leah et al., 2020), are evidence of fluid flow and a direct structural link to the late-stage upward growth of the polygonal faults. Some of these fault structures may have formed during early stages of slow pelagic sedimentation.

Comparable layer-bound compactional fault systems have rarely been reported from subduction margins or subducting plates (Cartwright, 2011; Tilley et al., 2021). Heffernan et al. (2004) identified well-developed polygonal faults in the ~500-m-thick incoming mudstones of the Shikoku Basin outboard of the Nankai subduction zone. Based on the distribution of these faults revealed by 3D seismic data, they inferred the faults to be caused primarily by differential compaction and dewatering of the fine-grained sediments overlying an irregular oceanic basement. They also considered that secondary compaction results from loading of the incoming sequence by the front of the accretionary wedge.

6.2. Implications for subduction processes

Using seismic data tied to borehole logs and core data from IODP Site U1520, Barnes et al. (2020) inferred that the shallow subduction interface in the SSE source area likely comprises an assemblage of mixed lithologies derived from the calcareous pelagic and volcaniclastic units. They argued that shallow plate interface SSEs are influenced by the heterogenous lithological, mechanical, and frictional properties of the fault zone materials at a variety

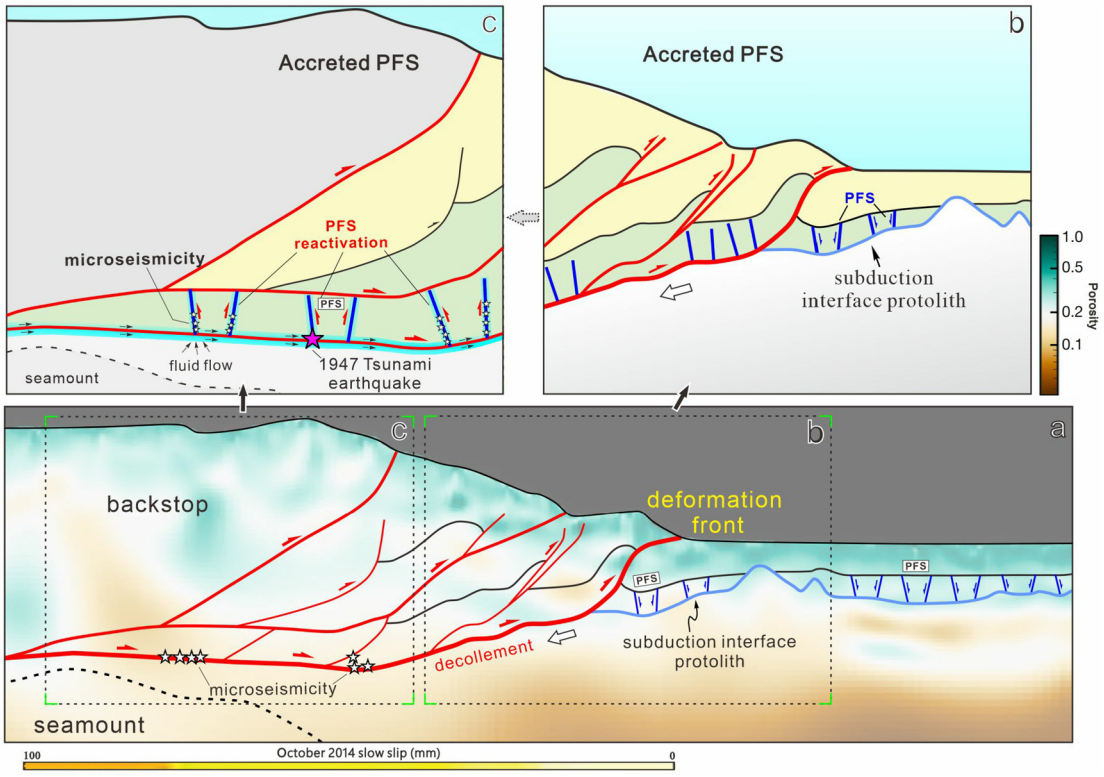

Fig. 9. a) Structural interpretation emphasizing the PFS in the incoming sequence (modified from Barnes et al., 2020), overlying porosity structure derived from passive and controlled-source seafloor electromagnetic data collected at the northern Hikurangi Margin from Chesley et al. (2021). b) Polygonal faults transported into the accretionary wedge. c) Schematic illustration of inferred PFS reactivation associated with fluid flow, microearthquakes, and tremor in the lower accretionary wedge.

of scales and are enhanced by the high relief on the subducted oceanic crust. These findings supported earlier suggestions from modeling and laboratory experiments that shallow, slow slipping subduction fault zones with transitional frictional stability may be associated with tectonic mélange containing variable mixtures of velocity-strengthening and velocity-weakening materials (e.g., Fagereng and Sibson, 2010; Saffer and Wallace, 2015; Boulton et al., 2019). Leah et al. (2020) suggested that weak sub-horizontal stylolites and clusters of faults, fractures, and phyllosilicate-rich seams in the otherwise strong incoming carbonates may localize slip where the plate interface intersects these rocks and may contribute to local perturbations in the geometry of the interface slip surfaces.

We consider that seismic-scale polygonal fault development in the pelagic section potentially influences subduction zone processes in three additional ways. Firstly, the PFS could potentially influence the frictional behavior of the plate interface by promoting incorporation of the pelagic sediments into the shallow plate-boundary fault zone and contributing to the compositional and geometric heterogeneity of the interface (Leah et al., 2020; Barnes et al., 2020). A recent frictional study using rock samples collected during IODP Expedition 375, showed that the calcite-rich pelagic unit (Unit IV, 510-848 mbsf) is a likely candidate to host shallow SSEs observed at the margin (Eijsink and Ikari, 2022). The SSEs spontaneously produced in the laboratory with partial locking in between sliding events observed in the calcareous pelagic samples from Unit IV are consistent with the interpretation of SSEs within the spectrum of slow to fast earthquakes. Secondly, a considerable volume of the pelagic calcareous sequence is accreting into the northern (Fagereng et al., 2019; Barnes et al., 2020) and central (Barnes et al., 2020; Ghisetti et al., 2016; Barnes et al., 2019) Hikurangi accretionary wedge. We suggest that favorably oriented normal faults, and particularly those with modest dips, may provide inherited structural weaknesses suitable for compressional reactivation and inversion within the lower wedge (Fig. 9), thus contributing to both the structural architecture of the wedge and the accommodation of stresses associated with subducting seamounts (e.g., Ruh et al., 2016; Sun et al., 2020). Thirdly, we suggest that selective reactivation of the polygonal faults and associated fractures in the pelagic calcareous section as part of ongoing volumetric deformation within the lower wedge may retain or re-open fracture permeability and facilitate upward fluid flow associated with expulsion from the lower wedge or transient leakage from underlying subducting sediment across the subduction interface (Fig. 9c). Such leakage may be critical in modulating fluid pressure and transient slip within the subduction interface fault zone (e.g., Saffer and Tobin, 2011; Saffer and Wallace, 2015; Warren-Smith et al., 2019), while upwards fluid migration through the hanging wall may be associated with seismic phenomena in the accretionary wedge, including tremor, microseismicity, and transient pulsing of fluid overpressure (e.g., Schwartz and Rokosky, 2007; Ellis et al., 2015; Todd et al., 2018; Barker et al., 2018; Chesley et al., 2021) (Fig. 9).

7. Conclusions

Regional seismic reflection profiles and drilling data from IODP Expeditions 372 and 375 from the northern Hikurangi Trough, New Zealand, reveal the initial compactional deformation of incoming pelagic sedimentary sequences of the subducting plate seaward of the deformation front.

1) We report a network of layer-bound polygonal faults at seismic scale that are centered in the Paleocene to Miocene pelagic carbonate and calcareous mudstone units and locally extend into the lower components of the overlying siliciclastic section. 3D seismic coherence slice and 2D seismic reflection profile analyses reveal the polygonal structure of these faults and

acoustic evidence of fault-related fluid migration. These faults exhibit stratigraphic and structural attributes that are typical of PFSs observed globally, mainly from sedimentary basins undergoing compactive deformation on passive continental margins, and rarely reported elsewhere at subduction zones.

2) The seismic reflection data indicate low finite fault displacements (typically < 30 m). The seismic-scale fault displacements and growth strata are consistent with fault nucleation at shallow stratigraphic levels and contemporary seafloor deformation, followed by progressive upwards and downwards propagation of fault tips coeval with syn-kinematic deposition. Two groups of displacement profiles are recognized, locally correlating to lateral variations in seismic amplitudes. Based on these observations, coupled with weak correlations in specific fault growth intervals and throw rates across the PFS, we speculate that spatial and stratigraphic variability in the development of specific faults and polygonal cells may be affected by lateral variations in physical properties. In support of studies reported elsewhere, we find that the polygonal faults formed at extremely slow rates, with an increase in slip rate from 0.5-3 m/Ma during pelagic sedimentation to about 20 m/Ma following the onset of siliciclastic sedimentation.
3) We suggest that downdip within the subduction zone the polygonal faults in the incoming pelagic sediments may influence the properties of the plate interface and the structural deformation and evolution of the over-riding accretionary wedge. Reactivation of these inherited compactive structures within the lower wedge may retain or re-open fracture permeability and facilitate upward fluid flow associated with expulsion from the lower wedge or transient leakage across the subduction interface, processes that have been suggested to explain seismic phenomena at northern Hikurangi including seismic tremor and burst-type repeating earthquakes (Todd et al., 2018; Shaddox and Schwartz, 2019). We suggest that these structural features inherited from the incoming sedimentary sequence, and their possible influence on shallow subduction mechanics and accretionary wedge evolution may be under-appreciated at other subduction zones, for example in Ryukyu Trench and Nankai Trough (e.g., Tilley et al., 2021), where significant fine-grained pelagic sediments occur in the incoming plate sedimentary succession, and in particular where thick sections of carbonate and calcareous mudstone rocks are present.

CRediT authorship contribution statement

Maomao Wang: Conceptualization, Formal analysis, Funding acquisition, Investigation, Writing – original draft, Writing – review & editing. **Philip M. Barnes:** Conceptualization, Formal analysis, Funding acquisition, Writing – original draft, Writing – review & editing. **Julia K. Morgan:** Conceptualization, Formal analysis, Writing – review & editing. **Rebecca E. Bell:** Formal analysis, Funding acquisition, Writing – review & editing. **Gregory F. Moore:** Formal analysis, Funding acquisition, Writing – review & editing. **Ming Wang:** Formal analysis, Writing – review & editing. **Ake Fagereng:** Formal analysis, Funding acquisition, Writing – review & editing. **Heather Savage:** Formal analysis, Writing – review & editing. **Davide Gamboa:** Formal analysis, Writing – review & editing. **Robert N. Harris:** Formal analysis, Writing – review & editing. **Stuart Henrys:** Formal analysis, Funding acquisition, Writing – review & editing. **Joshu Mountjoy:** Formal analysis, Funding acquisition, Writing – review & editing. **Anne M. Tréhu:** Formal analysis, Writing – review & editing. **Demian Saffer:** Formal analysis, Writing – review & editing. **Laura Wallace:** Formal analysis, Writing – review & editing. **Katerina Petronotis:** Formal analysis, Funding acquisition, Writing – review & editing.

Declaration of competing interest

The authors declare that they have no known competing financial interests or personal relationships that could have appeared to influence the work reported in this paper.

Data availability

Processed seismic reflection data of TAN1114 and RR1508 can be found at: Zenodo: https://doi.org/10.5281/zenodo.6758019.

Acknowledgements

This research used samples and data provided by the International Ocean Discovery Program. We thank the staff onboard the RV JOIDES Resolution during IODP Expeditions 372 and 375 for their support. M. Wang was supported by National Key R&D Program of China (2021YFC3000604) and the NSFC (42172232). P. Barnes, J. Mountjoy and S. Henrys were supported by the New Zealand MBIE Endeavour Fund Contract CO5X1605, NIWA and GNS Science SSIF core funding. Support was provided to K. Petronotis by IODP-JRSO NSF Award 1326927, to R. Bell and A. Fagereng by NERC awards NE/S00291X/1 and NE/S002731/1, to G. Moore by NSF award OCE-2023186, and to D. Gamboa by the FCT I.P./MCTES through funds (PIDDAC) UIDB/50019/2020 and by FCT project PTDC/CTA-GEO/30381/2017. Cruise TAN1114 was supported by the New Zealand Government Ocean Survey 2020 grant. We thank the captain and crew of RV *Tangaroa* for support during TAN1114. Cruise RR1508 was funded by NSF grants OCE-1355878 and OCE-1355870 to R. Harris, A. Tréhu. We thank Nathan Bangs, University of Texas, for permission to present the 2018NZ3D seismic data, and two anonymous reviewers for their constructive reviews.

Appendix A. Supplementary material

Supplementary material related to this article can be found online at https://doi.org/10.1016/j.epsl.2023.118022.

References

Bahorich, M., Farmer, S., 1995. 3-D seismic discontinuity for faults and stratigraphic features: the coherence cube. Lead. Edge 14 (10), 1053–1058.

Barker, D.H., Henrys, S., Caratori Tontini, F., Barnes, P.M., Bassett, D., Todd, E., Wallace, L., 2018. Geophysical constraints on the relationship between seamount subduction, slow slip, and tremor at the north Hikurangi subduction zone, New Zealand. Geophys. Res. Lett. 45 (23), 12–804.

Barnes, P.M., Lamarche, G., Bialas, J., Henrys, S., Pecher, I., Netzeband, G.L., Greinert, J., Mountjoy, J.J., Pedley, K., Crutchley, G., 2010. Tectonic and geological framework for gas hydrates and cold seeps on the Hikurangi subduction margin, New Zealand. Mar. Geol. 272 (1–4), 26–48.

Barnes, P.M., Wallace, L.M., Saffer, D.M., Pecher, I.A., Petronotis, K.E., LeVay, L.J., 2019. The Expedition 372/375 Scientists Site U1520. In: Wallace, L.M., Saffer, D.M., Barnes, P.M., Pecher, I.A., Petronotis, K.E., LeVay, L.J. (Eds.), Hikurangi Subduction Margin Coring, Logging, and Observatories. Proceedings of the International Ocean Discovery Program, 372B/375, College Station, TX.

Barnes, P.M., Wallace, L.M., Saffer, D.M., Bell, R.E., Underwood, M.B., Fagereng, A., Meneghini, F., Savage, H.M., Rabinowitz, H.S., Morgan, J.K., Kitajima, H., Kutterolf, S.O., Hashimoto, Y., Engelmann de Oliveira, C.H., Noda, A., Crundwell, M.P., Shepherd, L., Woodhouse, A.D., Harris, R.N., Wang, M., Henrys, S., Barker, D.H.N., Petronotis, K.E., Bourlange, S.M., Clennell, M.B., Cook, A.E., Dugan, B.E., Elger, J.E., Fulton, P.M., Gamboa, D., Greve, A., Han, S., Hüpers, A., Ikari, M.J., Ito, Y., Young Kim, G., Koge, H., Lee, H., Li, X., Luo, M., Malie, P.R., Moore, G.F., Mountjoy, J.J., McNamara, D.D., Paganoni, M., Screaton, E.J., Shankar, U., Shreedharan, S., Solomon, E.A., Wang, X., Wu, H-Y., Pecher, I.A., LeVay, L.J., IODP Expedition 372 Scientists, 2020. Slow slip source characterized by lithological and geometric heterogeneity. Sci. Adv. https://doi.org/10.1126/sciadv.aay3314.

Bell, R., Holden, C., Power, W., Wang, X., Downes, G., 2014. Hikurangi margin tsunami earthquake generated by slow seismic rupture over a subducted seamount. Earth Planet. Sci. Lett. 397, 1–9.

Berndt, C., Bünz, S., Mienert, J., 2003. Polygonal fault systems on the mid-Norwegian margin: a long-term source for fluid flow. Geol. Soc. (Lond.) Spec. Publ. 216 (1), 283–290.

Boulton, C., Niemeijer, A.R., Hollis, C.J., Townend, J., Raven, M.D., Kulhanek, D.K., Shepherd, C.L., 2019. Temperature-dependent frictional properties of heterogeneous Hikurangi Subduction Zone input sediments, ODP Site 1124. Tectonophysics 757, 123–139.

Boulton, C., Mizera, M., Niemeijer, A.R., Little, T.A., Müller, I.A., Ziegler, M., Hamers, M.F., 2022. Observational and theoretical evidence for frictional-viscous flow at shallow crustal levels. Lithos 106831.

Cartwright, J., 2011. Diagenetically induced shear failure of fine-grained sediments and the development of polygonal fault systems. Mar. Pet. Geol. 28 (9), 1593–1610.

Chesley, C., Naif, S., Key, K., et al., 2021. Fluid-rich subducting topography generates anomalous forearc porosity. Nature 595, 255–260. https://doi.org/10.1038/s41586-021-03619-8.

Collot, J.Y., Lewis, K., Lamarche, G., Lallemand, S., 2001. The giant Ruatoria debris avalanche on the northern Hikurangi margin, New Zealand: result of oblique seamount subduction. J. Geophys. Res., Solid Earth 106 (B9), 19271–19297.

Crundwell, M.P., Woodhouse, A., 2022. Biostratigraphically constrained chronologies for Quaternary sequences from the Hikurangi margin of north-eastern Zealandia. N.Z. J. Geol. Geophys. https://doi.org/10.1080/00288306.2022.2101481.

Crutchley, G.J., Klaeschen, D., Henrys, S.A., Pecher, I.A., Mountjoy, J.J., Woelz, S., 2020. Subducted sediments, upper-plate deformation and dewatering at New Zealand's southern Hikurangi subduction margin. Earth Planet. Sci. Lett. 530, 115945.

Davy, B., Hoernle, K., Werner, R., 2008. Hikurangi Plateau: crustal structure, rifted formation, and Gondwana subduction history. Geochem. Geophys. Geosyst. 9, Q07004.

Dutilleul, J., Bourlange, S., Géraud, Y., Stemmelen, D., 2020. Porosity, pore structure, and fluid distribution in the sediments entering the northern Hikurangi margin, New Zealand. J. Geophys. Res., Solid Earth 125, e2020JB020330.

Eichelberger, N.W., Nunns, A.G., Groshong, R.H., Hughes, A.N., 2017. Direct estimation of fault trajectory from structural relief. AAPG Bull. 101 (5), 635–653.

Eijsink, A.M., Ikari, M.J., 2022. Plate-rate frictional behavior of sediment inputs to the Hikurangi Subduction Margin: how does lithology control slow slip events? Geochem. Geophys. Geosyst. 23 (6), e2022GC010369.

Ellis, S., Fagereng, A., Barker, D., Henrys, S., Saffer, D., Wallace, L., Williams, C., Harris, R., 2015. Fluid budgets along the northern Hikurangi subduction margin, New Zealand: the effect of a subducting seamount on fluid pressure. Geophys. J. Int. 202, 277–297.

Fagereng, Å., Savage, H.M., Morgan, J.K., Wang, M., Meneghini, F., Barnes, P.M., et al., 2019. Mixed deformation styles observed on a shallow subduction thrust, Hikurangi margin, New Zealand. Geology 47 (9), 872–876.

Fagereng, Å., Sibson, R.H., 2010. Mélange rheology and seismic style. Geology 38 (8), 751–754.

Gase, A.C., Van Avendonk, H.J., Bangs, N.L., Bassett, D., Henrys, S.A., Barker, D.H., et al., 2021. Crustal structure of the northern Hikurangi margin, New Zealand: variable accretion and overthrusting plate strength influenced by rough subduction. J. Geophys. Res., Solid Earth 126 (5), e2020JB021176.

Gay, A., Lopez, M., Cochonat, P., Sermondadaz, G., 2004. Polygonal faults-furrows system related to early stages of compaction–upper Miocene to recent sediments of the Lower Congo Basin. Basin Res. 16 (1), 101–116.

Gay, A., Padron, C., Meyer, S., Beaufort, D., Oliot, E., Lallemand, S., et al., 2021. Elongated giant seabed polygons and underlying polygonal faults as indicators of the creep deformation of Pliocene to recent sediments in the Grenada Basin, Caribbean Sea. Geochem. Geophys. Geosyst. 22 (12), e2021GC009809.

Ghisetti, F.C., Barnes, P.M., Ellis, S., Plaza-Faverola, A.A., Barker, D.H., 2016. The last 2 Myr of accretionary wedge construction in the central Hikurangi margin (North Island, New Zealand): insights from structural modeling. Geochem. Geophys. Geosyst. 17 (7), 2661–2686.

Gratier, J.P., Dysthe, D.K., Renard, F., 2013a. The role of pressure solution creep in the ductility of the Earth's upper crust. Adv. Geophys. 54, 47–179. https://doi.org/10.1016/B978-0-12-380940-7.00002-0.

Gratier, J.P., Thouvenot, F., Jenatton, L., Tourette, A., Doan, M.L., Renard, F., 2013b. Geological control of the partitioning between seismic and aseismic sliding behaviours in active faults: evidence from the Western Alps, France. Tectonophysics 600, 226–242.

Gray, M., Bell, R.E., Morgan, J.V., Henrys, S., Barker, D.H., IODP Expedition 372 and 375 Science Parties, 2019. Imaging the shallow subsurface structure of the North Hikurangi Subduction Zone, New Zealand, using 2D full-waveform inversion. J. Geophys. Res., Solid Earth 124 (8), 9049–9074.

Han, S., Bangs, N.L., Hornbach, M.J., Pecher, I.A., Tobin, H.J., Silver, E.A., 2021. The many double BSRs across the Northern Hikurangi Margin and their implications for subduction processes. Earth Planet. Sci. Lett. 558, 116743. https://doi.org/10.1016/j.epsl.2021.116743.

Heffernan, A.S., Moore, J.C., Bangs, N.L., Moore, G.F., Shipley, T.H., 2004. Initial deformation in a subduction thrust system: polygonal normal faulting in the incoming sedimentary sequence of the Nankai subduction zone, southwestern Japan. Geol. Soc. Lond. Mem. 29 (1), 143–148.

Hoernle, K., Hauff, F., Van den Bogaard, P., Werner, R., Mortimer, N., Geldmacher, J., et al., 2010. Age and geochemistry of volcanic rocks from the Hikurangi and Manihiki oceanic Plateaus. Geochim. Cosmochim. Acta 74 (24), 7196–7219.

Hüpers, A., Torres, M.E., Owari, S., McNeill, L.C., Dugan, B., Henstock, T.J., et al., 2017. Release of mineral-bound water prior to subduction tied to shallow seismogenic slip off Sumatra. Science 356 (6340), 841–844.

Ikari, M.J., Niemeijer, A.R., Spiers, C.J., Kopf, A.J., Saffer, D.M., 2013. Experimental evidence linking slip instability with seafloor lithology and topography at the Costa Rica convergent margin. Geology 41 (8), 891–894. https://doi.org/10.1130/G33956.1.

King, J.J., Cartwright, J.A., 2020. Ultra-slow throw rates of polygonal fault systems. Geology 48 (5), 473–477.

Kirkpatrick, J.D., Edwards, J.H., Verdecchia, A., Kluesner, J.W., Harrington, R.M., Silver, E.A., 2020. Subduction megathrust heterogeneity characterized from 3D seismic data. Nat. Geosci. 13 (5), 369–374. https://doi.org/10.1038/s41561-020-0562-9.

Leah, H., Fagereng, Å., Meneghini, F., Morgan, J.K., Savage, H.M., Wang, M., et al., 2020. Mixed brittle and viscous strain localization in pelagic sediments seaward of the Hikurangi Margin, New Zealand. Tectonics 39 (8), e2019TC005965.

Lewis, K.B., Collot, J.Y., Lallem, S.E., 1998. The dammed Hikurangi Trough: a channel-fed trench blocked by subducting seamounts and their wake avalanches (New Zealand–France GeodyNZ Project). Basin Res. 10 (4), 441–468.

Moore, G.F., Tilley, H., Bangs, N., Han, S., 2021. Complex Stratigraphy on the Incoming Plate at the N. Hikurangi Margin from 3D Seismic Data. Am. Geophys. Union annual meeting, abstract # T42A-02.

Plank, T., 2014. The Chemical Composition of Subducting Sediments, second edition. Treatise on Geochemistry, vol. 4, pp. 607–629.

Plaza-Faverola, A., Klaeschen, D., Barnes, P., Pecher, I., Henrys, S., Mountjoy, J., 2012. Evolution of fluid expulsion and concentrated hydrate zones across the southern Hikurangi subduction margin, New Zealand: an analysis from depth migrated seismic data. Geochem. Geophys. Geosyst. 13 (8).

Rabinowitz, H.S., Savage, H.M., Skarbek, R.M., Ikari, M.J., Carpenter, B.M., Collettini, C., 2018. Frictional behavior of input sediments to the Hikurangi Trench, New Zealand. Geochem. Geophys. Geosyst. 19 (9), 2973–2990.

Ruh, J.B., Sallarès, V., Ranero, C.R., Gerya, T., 2016. Crustal deformation dynamics and stress evolution during seamount subduction: high resolution 3-D numerical modeling. J. Geophys. Res., Solid Earth 121, 6880–6902. https://doi.org/10.1002/2016JB013250.

Saffer, D.M., 2003. Pore pressure development and progressive dewatering in underthrust sediments at the Costa Rican subduction margin: comparison with northern Barbados and Nankai. J. Geophys. Res. 108 (B5), 2261. https://doi.org/10.1029/2002JB001787.

Saffer, D.M., Tobin, H.J., 2011. Hydrogeology and mechanics of subduction zone forearcs: fluid flow and pore pressure. Annu. Rev. Earth Planet. Sci. 39, 157–186.

Saffer, D.M., Wallace, L.M., 2015. The frictional, hydrologic, metamorphic and thermal habitat of shallow slow earthquakes. Nat. Geosci. 8, 594–600.

Scholl, D.W., Kirby, S.H., von Huene, R., Ryan, H., Wells, R.E., Geist, E.L., 2015. Great ($\geq$Mw8. 0) megathrust earthquakes and the subduction of excess sediment and bathymetrically smooth seafloor. Geosphere 11 (2), 236–265.

Schwartz, S.Y., Rokosky, J.M., 2007. Slow slip events and seismic tremor at circum-Pacific subduction zones. Rev. Geophys. 45, RG3004. https://doi.org/10.1029/2006RG000208.

Shaddox, H.R., Schwartz, S.Y., 2019. Subducted seamount diverts shallow slow slip to the forearc of the northern Hikurangi subduction zone, New Zealand. Geology 47 (5), 415–418.

Shillington, D.J., Bécel, A., Nedimović, M.R., Kuehn, H., Webb, S.C., Abers, G.A., et al., 2015. Link between plate fabric, hydration and subduction zone seismicity in Alaska. Nat. Geosci. 8 (12), 961–964.

Shreedharan, S., Ikari, M., Wood, C., Saffer, D., Wallace, L., Marone, C., 2022. Frictional and lithological controls on shallow slow slip at the northern Hikurangi margin. Geochem. Geophys. Geosyst. 23 (2), e2021GC010107.

Spinelli, G.A., Wang, K., 2008. Effects of fluid circulation in subducting crust on Nankai margin seismogenic zone temperatures. Geology 36 (11), 887–890.

Sun, T., Saffer, D., Ellis, S., 2020. Mechanical and hydrological effects of seamount subduction on megathrust stress and slip. Nat. Geosci. 13 (3), 249–255.

Tesei, T., Collettini, C., Barchi, M.R., Carpenter, B.M., Di Stefano, G., 2014. Heterogeneous strength and fault zone complexity of carbonate-bearing thrusts with possible implications for seismicity. Earth Planet. Sci. Lett. 408, 307–318.

Tilley, H.L., Moore, G.F., Yamashita, M., Kodaira, S., 2021. Along-strike variations in protothrust zone characteristics at the Nankai Trough subduction margin. Geosphere 17 (2). https://doi.org/10.1130/GES02305.1.

Todd, E., Schwatz, S., Williams, C., Sheehan, A., Mochizuki, K., Henrys, S., et al., 2018. Earthquakes and tremor linked to seamount subduction during shallow slow slip at the Hikurangi margin, New Zealand. J. Geophys. Res., Solid Earth 123, 6769–6783. https://doi.org/10.1029/2018JB016136E.

Underwood, M.B., 2007. Sediment inputs to subduction zones: why lithostratigraphy and clay mineralogy matter. In: Dixon, T.H., Moore, J.C. (Eds.), The Seismogenic Zone of Subduction Thrust Faults. Columbia Univ. Press, New York, pp. 42–85.

Viti, C., Collettini, C., Tesei, T., 2014. Pressure solution seams in carbonatic fault rocks: mineralogy, micro/nanostructures and deformation mechanism. Contrib. Mineral. Petrol. 167 (2), 1–15.

Wallace, L.M., 2020. Slow slip events in New Zealand. Annu. Rev. Earth Planet. Sci. 48, 175–203.

Wallace, L.M., Saffer, D.M., Barnes, P.M., Pecher, I.A., Petronotis, K.E., LeVay, L.J., 2019. The Expedition 372/375 Scientists Site U1520. In: Wallace, L.M., Saffer, D.M.,

Barnes, P.M., Pecher, I.A., Petronotis, K.E., LeVay, L.J. (Eds.), Hikurangi Subduction Margin Coring, Logging, and Observatories. Proceedings of the International Ocean Discovery Program, 372B/375, College Station, TX.
Wang, K., Bilek, S.L., 2011. Do subducting seamounts generate or stop large earthquakes? Geology 39 (9), 819–822.
Warren-Smith, E., Fry, B., Wallace, L., Chon, E., Henrys, S., Sheehan, A., et al., 2019. Episodic stress and fluid pressure cycling in subducting oceanic crust during slow slip. Nat. Geosci. 12 (6), 475–481.
Watterson, J., Walsh, J., Nicol, A., Nell, P.A.R., Bretan, P.G., 2000. Geometry and origin of a polygonal fault system. J. Geol. Soc. 157 (1), 151–162.